Research Article Vol. 14, No. 4 / 1 Apr 2024 / Optical Materials Express 847
Optical Materials EXPRESS

Effective medium metasurfaces using nanoimprinting of the refractive index: design, performance, and predictive tolerance analysis

MATTHEW PANIPINTO AND JUDSON D. RYCKMAN*

Holcombe Department of Computer and Electrical Engineering, Clemson University, Clemson, SC, 29634, USA
*jryckman@clemson.edu

Abstract: Production of flat optics incorporating subwavelength features, particularly at visible frequencies, remains a significant challenge. Here, we establish a framework for the design of effective medium metasurfaces (EMM), relying on nanoimprinting of mesoporous silicon to realize a patterned refractive index n(x,y) corresponding to an arbitrary transmitted phase profile ϕ(x,y). The method is used to design the stamp profile required to produce a Fresnel lens and the theoretical performance of the metalens is examined using the finite-difference time-domain method. Additionally, we demonstrate neural network aided Monte Carlo analysis as a method to model the effects of metasurface fabrications errors on EMM performance and process yield.

1. Introduction

Metasurfaces, artificial 2D structures with engineered properties, have enabled unprecedented control of light in the last decade [1–3]. Much of the early research in optical metasurfaces centered around the use of arrays of resonant scatterers [4–7]. An alternative to the resonant meta-atom approach is to use effective medium theory (EMT), which applies for a normally incident plane wave when the local periodicity Λ is subwavelength, e.g. $\Lambda < \lambda_0/n$ [8–10]. Effective medium metasurfaces (EMMs) can therefore be realized by patterning the shape, size, orientation, and/or composition of subwavelength dielectric nanostructures [11]. EMMs have now been realized using a variety of nanostructure geometries ranging from raised structures such as pillars and fins, to recessed structures including trenches and holes [12–15]. Many of these subwavelength geometries are favorable platforms for realizing future dynamic metasurfaces and metasurface-based sensors through the embedding of active materials within voids or holes in the subwavelength structure [16,17]. However, the scalable and cost-effective nanomanufacturing of such optical metasurfaces remains a significant challenge and an active area of investigation owing to the demand for patterning subwavelength dimensions across large areas.

It is well known that the fabrication of devices through direct writing strategies such as electron beam lithography (EBL), focused ion-beam milling (FIB), or similar methods, limits throughput as the critical dimension of the device decreases [18,19]. This tradeoff between throughput and resolution presents a significant hurdle to large scale production of subwavelength metasurfaces operating at optical frequencies. Prospective solutions to this tradeoff include nanomanufacturing strategies based on deep ultra-violet (DUV) lithography and nanoimprint lithography (NIL). For example, recent works have successfully demonstrated full wafer scale meta-optics using $\lambda = 248$ nm DUV lithography with a minimum feature size of ~250 nm. However, significant visible wavelength performance degradations were observed and attributed to the limited feature size which resulted in incomplete phase coverage and limited diffraction efficiency [20]. DUV at $\lambda = 193$ nm or extreme ultra-violet (EUV) at $\lambda = 13.5$ nm have been proposed as potential solutions to achieve higher resolution and better performance, however the practical and economic viability of deploying these methods for meta-optics remains unclear [21,22].

#515617 https://doi.org/10.1364/OME.515617
Journal © 2024 Received 2 Jan 2024; revised 22 Feb 2024; accepted 24 Feb 2024; published 4 Mar 2024

Optical Materials EXPRESS

Nanoimprinting is a promising alternative fabrication strategy since it can rapidly replicate nanoscale features without relying on direct-writing or diffraction limited optics. The most popular forms of NIL rely on either thermal or ultra-violet (UV) curing of a resist layer which is imprinted by a reusable mold or soft stamp. To date, a variety of works have now explored or demonstrated NIL based metasurfaces and meta-optics [23–27]. Typically, nanoimprinting must be followed by conventional additive or subtractive processes (e.g. film deposition or reactive ion etching), which increases process complexity and cost.

Alternatively, direct nanoimprinting offers a simple, rapid, and low-cost route to metasurface patterning. In one recent work, a 'plum pudding' metasurface was directly fabricated by imprinting a UV-curable resin loaded with TiO_2 nanoparticles [28], while in another work used atomic layer deposition of TiO_2 on top of a UV-curable resin was also demonstrated to enhance refractive index [27]. Other materials such as ZrO_2 have been posited as replacements for TiO_2 inclusions in nanocomposite-based EMMs [29]. However, these examples are limited to the synthesis of polymeric and thermoplastic nanocomposite-based metasurfaces, which may be limited to high aspect ratio structures and/or geometric phase due to the limited index contrast. Other variants of direct nanoimprinting have been demonstrated in materials with improved hardness and durability, including ultra-fast liquefaction of silicon [30], electrochemical nanoimprinting of silicon [31,32], and extreme pressure imprinting of Ni, steel, and Au [33]. However, such materials are not suitable for transparent meta-optics.

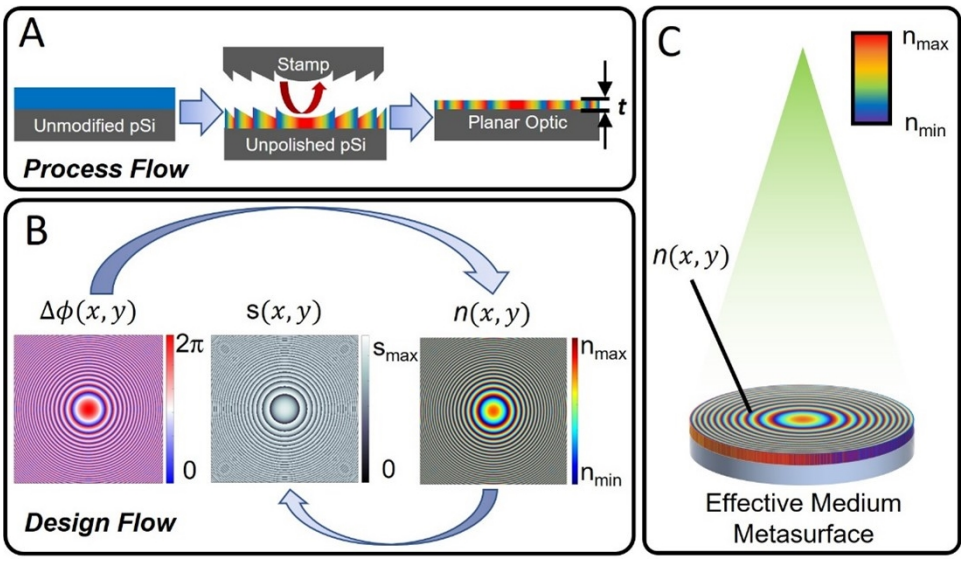

Fig. 1. (a) The NIRI process flow, in which an unpolished film of pSi on a Si substrate is first stamped with a pattern to impart a transverse refractive index profile through compression of the pSi substrate. The stamped pSi is then polished to a specific thickness to produce a planar effective medium metasurface. (b) The process flow described in this paper, which is used to create a NIRI stamp. An arbitrary phase profile is used to generate a refractive index profile, which is then used to design a stamp capable of imprinting the pSi substrate. (c) Illustration of an effective medium metasurface created using the NIRI process.

Our group has recently shown that direct imprinting of mesoporous silicon (pSi) can be utilized to directly pattern spatially variant digital or analog refractive index profiles $n(x,y) = n_0 + \Delta n(x,y)$ on the surface of a chip in a process referred to as 'nanoimprinting refractive index' (NIRI) [34]. The NIRI process and its application toward meta-optic fabrication are illustrated in Fig. 1. While our prior experimental work demonstrated NIRI's utility in fabricating visible and near-infrared

Optical Materials EXPRESS

wavelength EMMs, e.g. realizing a low numerical aperture (NA) gradient refractive index metalens and metamaterial waveguides, several additional challenges and open questions related to NIRI patterning must be investigated before it can be deployed for nanomanufacturing of custom designed meta-optics. Key items to investigate include: (1) the design of full 2π phase transmissive metasurfaces based on a patterned refractive index distribution $n(x,y)$, (2) the design and generation of a corresponding 3D stamp/master required for imprinting the meta-optic, (3) understanding the theoretical performance of NIRI based EMMs, e.g. using a metalens as a prototypical structure, both under ideal fabrication conditions, and (4) when fabrication variations and non-idealities are present.

In this work, we investigate and address each of these four key items. Firstly, we design NIRI compatible meta-lenses using full 2π phase control based on the experimentally achievable refractive index contrast of the NIRI process ($\Delta n \approx 1$ RIU). Next, we solve the inverse design problem of mapping the desired phase profile $\Delta\phi(x,y)$ first to the required EMM index distribution $n(x,y)$ and finally to the required stamp height profile $s(x,y)$ as illustrated in Fig. 1(b). This allows for the automated design generation of arbitrary stamp height profiles $s(x,y)$ using only an input phase function $\Delta\phi(x,y)$ and knowledge of the initial pSi thickness h_0 and initial pSi porosity P_0. Lastly, we numerically evaluate the performance of NIRI based meta-optics using finite difference time domain (FDTD) simulation. To investigate process tolerance and predict real world manufacturability, we perform a Monte Carlo (MC) simulation and develop a predictive neural network model that factors in the primary sources of fabrication variation.

2. EMM design and performance analysis

2.1. Approach

As illustrated in Fig. 1(a), the NIRI patterning process uses a premastered and reusable hard stamp to impart a localized change in the refractive index Δn(x,y) of a porous silicon film through compression [35]. Previous works related to the NIRI technique have used a hard stamp fabricated either in Si or SiO_2, with Si stamps typically being easier to prototype but SiO_2 stamps being more durable. Previous work has demonstrated that a hard SiO_2 stamp can produce more than 50 imprints before requiring replacement [34]. After imprinting, the compressed pSi film is subsequently polished to a final desired thickness *t,* such that phase imparted onto an incident plane-wave is directly controlled by the effective refractive index profile n(x,y) of the flat optic, with a planar optic being necessary due to the direct trade-off between n and t. Without planarization, thick regions would have low n and thin regions would have high n. A 2π phase contrast is much more easily achieved when t is set to a constant value. To achieve 2π phase control at a given wavelength λ_0, the post-polish planar thickness t must be chosen such that the light transmitted through the device has the same phase when $n(x,y) = n_{min}$ and n_{max}. Since NIRI has been demonstrated to impart maximum $\Delta n \approx 1$, it is expected that the final flat optic will have a post-polish planar thickness $t \approx \lambda_0$ for a transmissive EMM [35]. We note that this thickness is ~3-4x thinner than recent EMMs based on high-aspect ratio holes etched into silicon where $\Delta n \approx 0.3$ and is comparable in thickness to nano-finned EMMs which typically require EBL patterning of high-aspect ratio (~1:7) nano-fins [14,36].

Whereas traditional metasurface design requires mapping the desired phase profile to the geometrical properties of the local meta-atoms, NIRI based EMMs require solving for the stamp height profile s(x,y) that will be used in the imprinting process. Here, we address this specific design problem. As illustrated in Fig. 1(b), the input phase profile $\Delta\phi$(x,y) is first mapped to the target refractive index profile $n(x,y)$ assuming a nominal post-planarization thickness t. Then the post-imprint refractive index profile is mapped to the required stamp height profile s(x,y). These steps are carried out as detailed in the following section.

Optical Materials EXPRESS

2.2. Solving for the stamp design

To design a stamp capable of imparting an arbitrary phase function into a pSi film, we map three key relationships: (1) film compression vs. stamp height, (2) effective refractive index n vs. transmitted phase $\Delta\phi$ as shown in Fig. 2(a), and (4) effective refractive index vs. film compression as shown in Fig. 2(b). As illustrated in Fig. 2(a), the transmitted phase increases monotonically with effective refractive index. Here, the transmitted phase is calculated using the transfer matrix method (TMM), which is chosen for its low computational overhead and ability to accurately compute the phase accumulation of a plane wave transmitted through layered films [37]. The TMM is used assuming an operating wavelength $\lambda_0 = 532$ nm, a polished final film thickness $t = 466$ nm, an air top cladding and a substrate refractive index $n_{sub} = 1.74$. A linear fit of Fig. 2(a) agrees with the expected transmissive phase response: $\Delta\phi = 2\pi/\lambda_0 \times (n - n_0) \times t$, with a maximum observed residual of ≈67 mrad.

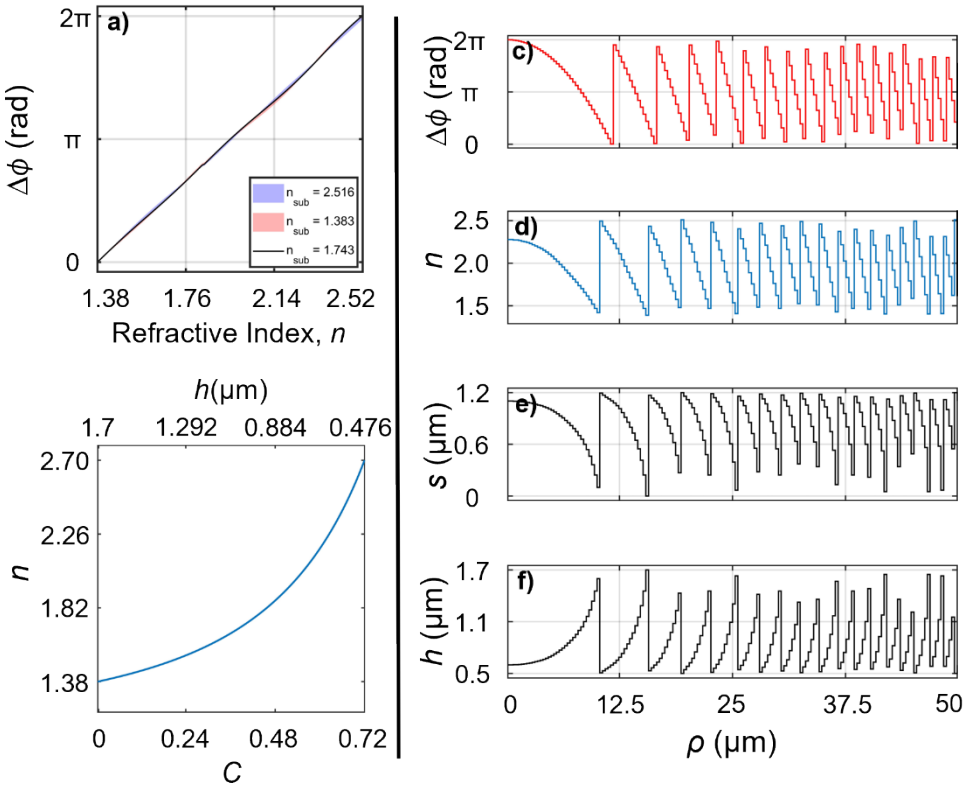

Fig. 2. (a) Relationship between refractive index and transmitted phase as calculated by TMM assuming a polished film thickness of 466 nm and an operating wavelength $\lambda_0 = 532$ nm. The dashed red line indicates the post-polish thickness t required to achieve $\Delta\phi = 2\pi$. (b) Relationship between refractive index, compression C, and post-imprint film thickness t for a pSi film with initial porosity $P_0 = 0.72$ and initial thickness $h_0 = 1.7$ μm. Compression is shown on the bottom x-axis with post-imprint film thickness shown on the top x-axis. (c-f) The workflow used to design a 100 μm diameter Fresnel lens with a focal length $f = 125$ μm at $\lambda_0 = 532$ nm: (c) the input phase profile digitized to 224 phase levels with 300 nm spatial resolution, (d) radial refractive index distribution, (e) required stamp design, and (f) the post-imprint film thickness h.

Figure 2(b) illustrates the relationship between film compression and refractive index for an initial pSi thickness $h_0 = 1.7$ μm thick pSi layer with initial pSi porosity $P_0 = 0.72$. This effective

Optical Materials EXPRESS

index vs. film compression model was derived and empirically calibrated in prior experimental works which established the relationship between film compression and effective refractive index for mesoporous silicon films with initial pSi porosity $P_0 = 0.72$ and a skeleton comprised of ~50:50 Si:SiO_2 [34,35]. In practice, such pSi films can be prepared by electrochemical etching of highly p-doped 0.01-0.02 Ohm-cm <100> silicon wafers in 15% ethanoic hydrofluoric acid to a desired pre-imprint film thickness, which in this work is set to $h_0 = 1.7$ µm.

As indicated in Fig. 2(b) the minimum pre-polish pSi height h value required to achieve 2π phase coverage is $h_{min} = 540$ nm. This corresponds to a maximum film compression $C_{max} = (h_0 - h_{min})/h_0 = 0.68$, with film compression generally given by $C = -\Delta h/h_0$. This compression corresponds to a required maximum stamp height $s_{max} = h_0 - h_{min} = 1.16$ µm. To ensure manufacturability, it is crucial that the maximum compression is less than the initial void fraction, $C_{max} < P_0$. Unannealed structures in the "over-stamped" regime may be removed during ultra-sonification or cleaning processes [34,38]. Annealed devices are more resistant to this deformation, as will be considered in a later section in which the performance of both annealed and unannealed lenses will be evaluated.

To design a stamp capable of imparting an arbitrary phase function into a pSi film, the pSi film compression that achieves $\Delta\phi = 2\pi$ is first calculated using TMM and then discretized into a depth vector $\mathbf{d}$ with i discrete values such that $0 \le \mathbf{d}_i \le \mathbf{d}_0$ where bold script has been used to indicate discretized vectors. The compression required to produce each value of $\mathbf{d}$ is then used to create a refractive index vector $\mathbf{n}$ using the three-component Bruggeman model and a phase vector $\mathbf{p}$ using TMM. The desired optic is represented as a phase function $\Delta\phi$(x,y) of arbitrary size and resolution. Each point of $\Delta\phi$(x,y) is matched to a corresponding value of $\mathbf{p}$ using a nearest-neighbor approach, resulting in a mapped phase function that approximates $\Delta\phi$(x, y) according to $\mathbf{p}$. The resultant mapped phase is then matched to its corresponding refractive index value in $\mathbf{n}$ and the associated final film height required to create the necessary refractive index at $n(x,y)$. This allows $\Delta\phi$(x,y) to be mapped to a pre-polish spatial height map h(x,y). The relief profile can then be taken as the required stamp height profile s(x,y):

$$s(\mathrm{x}, \mathrm{y}) = h_0 - h(x, y) \tag{1}$$

Aside from numerically determining the required stamp profile via this technique, we note that an analytic solution can be derived by applying EMT to the pSi film under compression, while maintaining the assumption of zero-Poisson ratio [34]:

$$s(x,\ y) = h_0 \left(1\ -\ \frac{1 - P_0}{1 - P(x,\ y)}\right), \tag{2}$$

where P(x,y) is the targeted spatial porosity distribution. As reported in the Appendix, Eq. (2) can be expanded by employing Bruggeman EMT to replace the porosity terms with refractive index terms. We note however, that the numerical approach presented here inherently utilizes the spatial film porosity P(x,y) and EMT which allows for correctly capturing the complex refractive index $\tilde{n} = n + ik$ for any compression or film thickness. As such all modelling in this work is performed using the numerical method, which accounts for both phase modulation and the small amount of absorption loss present in the films. The approach offered in the Appendix is reported here for completeness and can be used as an alternative means to approximate the required stamp design from a given arbitrary phase profile.

2.3. Flat lens design and performance

To examine the theoretical performance of a NIRI based transmissive EMM, we choose a flat Fresnel lens as a prototypical metasurface. The Fresnel lens is chosen due to its ubiquity in metasurface research in addition to its analytic phase function. The Fresnel lens is described by a

Optical Materials EXPRESS

phase function:

$$\Delta\phi(x, y) = \frac{-2\pi}{\lambda_0}\left(\sqrt{\rho(x, y)^2 + f^2} - f\right) \tag{3}$$

Here, ρ(x,y) is the radius from the center of the lens, f is the focal length and λ_0 is the incident wavelength.

Figure 2(c)-(f) depicts the process for designing a stamp to create a planar Fresnel lens using the previous equation with $f = 125$ µm, $\lambda_0 = 532$ nm and ρ_{max}(x,y) = 50 µm in a pSi film 1.7 µm thick with an initial pSi porosity $P_0 = 0.72$. This method can be used to design a stamp that can be used to compress a pSi film to fabricate a lens described by an arbitrary phase profile. To understand the theoretical performance characteristics of an optical device created using the NIRI process, we approximate the performance of the Fresnel lens in 2D and perform numerical simulation with Lumerical FDTD and application of Kirchhoff's integral. The lens is designed by simulating compression of a pSi film by a stamp designed as described above and using a post-polish thickness of 466 nm. Unless otherwise specified, the phase, refractive index and height vectors are all discretized to 224 possible values and the feature resolution is discretized to a pixel size of 300 nm × 300 nm. The simulated lens is considered to be supported by a 1 µm thick pSi substrate with the substrate porosity chosen to provide a refractive index value equal to the mean refractive index of all pixels comprising the lens in order to minimize Fresnel reflection. The lens is illuminated by monochromatic light with $\lambda_0 = 532$ nm in a radius of 37.5 µm, centered on the middle of the device.

Using this configuration, the actual focal distance f_{actual}, full width at half maximum (FWHM) and focusing efficiency η are calculated to be 125.14 µm, 0.95 µm and 0.952, respectively. η is taken here to be the ratio of power in an area three times the FWHM centered on the focal point over the transmitted power, given by:

$$\eta = \frac{P_{focal}}{P_{transmitted}} \tag{4}$$

Here, each metric can be used to assess lens performance from a different vantage point, with the actual focal distance representing the fidelity of the fabricated lens to the previously described Fresnel phase function, the FWHM describing the sharpness of the focal point, and η representing the overall effectiveness of the device in directing and focusing transmitted light.

A lens fabricated according to the design method described above has several degrees of freedom that can be adjusted to realize ideal performance parameters, including the baseline refractive index, voxel size and phase vector resolution. Baseline refractive index can be varied by adjusting the porosity of the initial pSi film by either modulating the current or adjusting the HF mixture in the porosification process, while voxel size is limited by the stamp fabrication process. In the design process, the discretization of the phase can be modulated up or down to either improve performance or to simplify fabrication. We also note that the maximum NA will ultimately be limited by the maximum refractive index gradient or phase gradient that can be realized in practice [39]. In this work we consider an NA = 0.29 metalens which would require minimum features comparable to a ~1.45 µm period blazed grating, which is expected to be well within the limits of the NIRI process.

Figure 3(a) reports the effect of modulating the number of phase levels on focusing efficiency η, while Fig. 3(b) reports a detailed visualization of the discretized refractive index profiles for selected phase resolutions. Corresponding simulations of electric field intensity are reported in Fig. 3(c). Here, we observe η is initially low (~0.18) in the case of 2 phase levels, but rapidly increases and plateaus to ~0.95 when the number of phase levels is increased to 16 or higher. This change in η in response to modulating the phase resolution is found to be consistent with diffraction theory which predicts $\eta_N = \eta_{max}$ $[\sin(\pi N)/(\pi N)]^2$, where is N the number of phase-levels [40,41].

Optical Materials EXPRESS

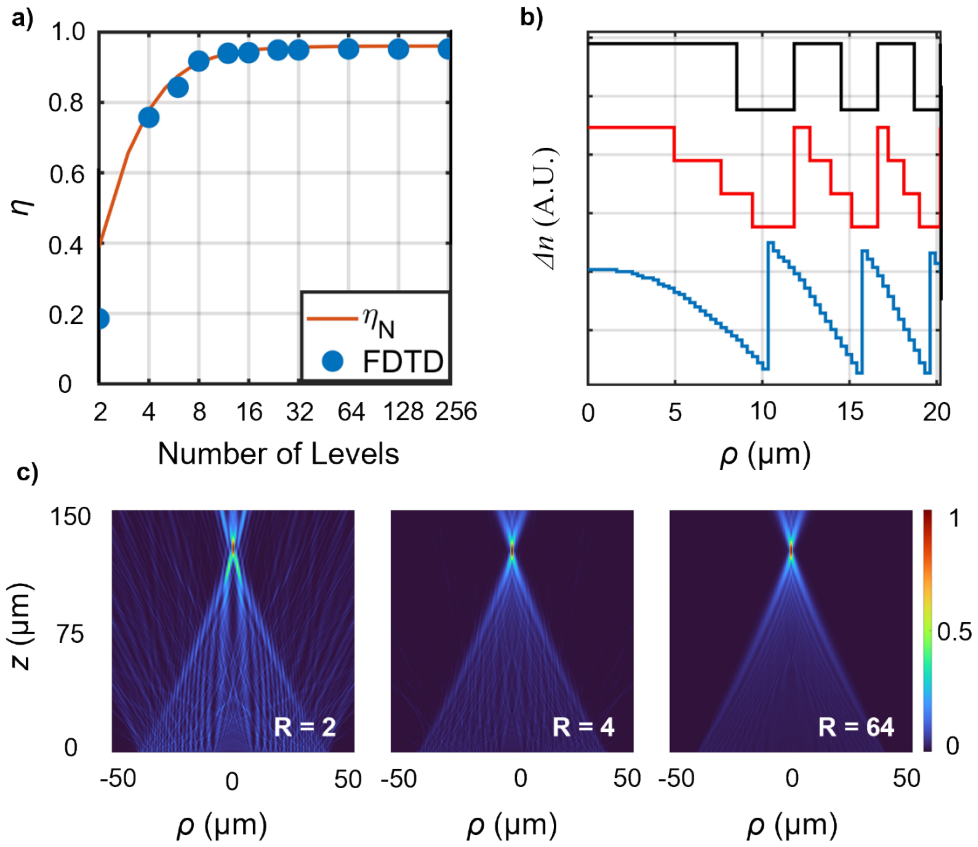

Fig. 3. (a) Simulated focusing efficiency η for Fresnel lenses with designed wavelength $\lambda_0 = 532$ nm and designed focal length $f = 125$ μm with varying phase resolutions used in the design process. (b) Refractive index profiles for devices designed with phase resolutions of 2, 4 and 64. (c) Simulated normalized electric field intensity for devices fabricated using phase resolutions of 2, 4, and 64.

While the focusing efficiency η approaches a theoretical maximum as the number of phase levels is increased, the transmission efficiency, T, of a NIRI based EMM will be affected by several additional factors. These factors include the operating wavelength, interfacial Fresnel reflection and transmission coefficients, fractional silicon composition and thickness of the film and any support layers. In prior experimental work we found the visible wavelength transmission efficiency to be primarily limited by the fractional silicon composition and film thickness [34]. In the present work, an upper bound on transmission efficiency $T_{max} = 0.85$ can be established from the average absorption coefficient of the polished film at 532 nm, which is estimated to be $\alpha \approx 0.3$ μm^{-1}. Assuming the EMM is placed on a transparent support layer, FDTD simulations indicate the total transmission efficiency to be ~0.75, which indicates Fresnel reflection loss is also non-negligible. For applications demanding maximum absolute transmission efficiency, addition of an anti-reflective coating could be utilized. Moreover, future work could potentially circumvent the visible wavelength absorption of pSi by advancing the application of NIRI with alternative mesoporous materials or nanocomposites such as those incorporating TiO_2.

Optical Materials EXPRESS

3. Fabrication tolerance

A comprehensive introduction to any novel fabrication is incomplete without a discussion of the errors that may arise in the fabrication process, including an analysis of the effects off those errors both individually and in concert. In addition to simulating the performance of an ideal NIRI Fresnel lens, a series of lenses with included fabrication errors are also simulated. These error simulations fall into two main categories: independently, where each of three fabrication defects is assessed individually, and interdependently, where the fabrication defects are re-examined as they occur simultaneously. The three dominant defects we examined are (1) post-planarization thickness, (2) imprinting depth, and (3) stamp height. An example of the effect of imprinting depth error on the refractive index profile of the designed lens can be seen in Fig. 4(a) while intensity profiles about the focal point of lenses with imprinting errors can be found in Fig. 4(b). The interplay of these errors is a complex, multivariable system that is investigated here using a Monte-Carlo analysis with results that are used as training data for a predictive neural network.

3.1. Independent defects

Errors in post-planarization thickness, incorrect stamp height, and improper imprint depth affect optical path length and thus the phase of transmitted light at the surface of the device. After imprinting, NIRI lenses undergo a chemical mechanical polishing (CMP) process to produce a planar optic [34]. Post-planarization thickness errors can be caused by an incorrectly executed polishing process, producing a planar EMM that is either too thick or too thin. Meanwhile, variations in stamp pressure, sample thickness, or Young's modulus can cause an error in the imprinting process, resulting in a correctly fabricated stamp that is pressed into the pSi film either too deeply or too shallowly. Fabricating a reusable stamp also requires the stamp to be etched in a Si or SiO_2 wafer. The abrupt height changes between $\Delta\phi(x,y) = 0$ and $\Delta\phi(x,y) = 2\pi$ requires an etching process that preserves aspect ratio while simultaneously having the correct etch selectivity. Stamp height errors can be caused by variations in grayscale lithography and/or etching processes, creating a stamp that is stretched or compressed in the z direction. Errors are simulated in a range that extends from $0.8\kappa \leq \kappa \leq 1.2\kappa$ in steps of 0.025κ, where $\kappa = 1$ is the ideal value for the lens characteristic in question. For the purposes of an independent error assessment, two errors are held to the ideal design values while the third error is varied through its simulation range.

Simulations are conducted and error examined in both annealed and unannealed lenses. Unannealed NIRI devices have been shown to crumble when compression reduces the pSi porosity to 0, resulting in the over-compressed pSi being removed during the ultrasonification process [34]. Annealed lenses are more resistant to this deformation. The results of the independently treated defects on η for both annealed and unannealed lenses can be seen in Fig. 4(c).

3.2. Interdependent defects and Monte Carlo analysis

While an independent examination of fabrication errors is useful in describing the errors and creating context for the fabrication process, a more complete picture of a fabricated lens requires that the defects presented be treated interdependently. In practical fabrication, simultaneous errors in the stamp profile, imprinting depth, and ideal post-polish thickness will be present in a NIRI lens to some degree and thus it is critical to understand the interplay between the three.

To create a more complete picture of the errors presented, a MC simulation is undertaken in which all three error ranges are randomized in a normal distribution with $3\sigma = 0.18$ about the ideal feature value. A sample of $N = 5000$ lenses with randomized defects is generated, simulated in Lumerical FDTD software and the results recorded. The results of the MC simulation yield a

Optical Materials EXPRESS

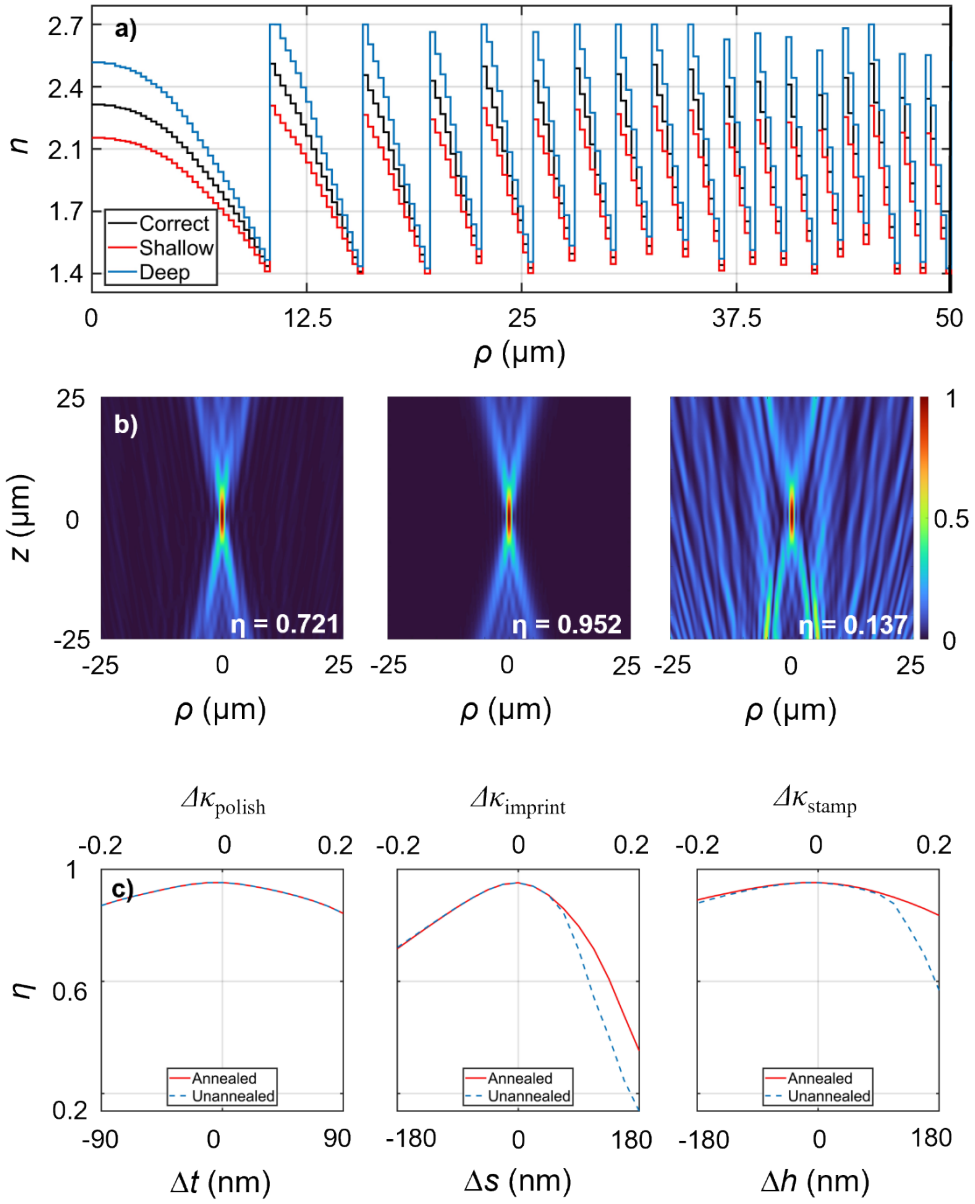

Fig. 4. (a) Calculated n for a radial slice of an unannealed version of the proposed lens when an ideal stamp has been imprinted correctly, too shallowly and too deeply. (b) Normalized electric field intensity about the focal points of the proposed lenses. From left to right, a shallow imprint, a correct imprint, and a deep imprint are demonstrated. Focusing efficiency η is given in the bottom right corner of each image. (c) From left to right, the simulated effects of incorrect post-polish optic height, incorrect imprinting depth, and incorrect stamp height on η for annealed and unannealed lenses. The deviation Δκ from the ideal values are given along the top x-axis, while the physical values associated with the deviations are given along the bottom x-axis.

Optical Materials EXPRESS

mean η of 0.82 with $\sigma_\eta = 0.17$, a mean f_{actual} of 125.03 μm with $\sigma_{focal} = 40.63$ nm, and a mean FWHM of 1.16 μm with $\sigma_{fwhm} = 3.26$ μm.

To extract meaningful data from the MC, lenses are divided into pass and fail categories. A lens is considered passing if $\eta \geq 0.9$ with a FWHM ≤ 1 μm. Using these constraints, 2261, or approximately 45%, of the 5,000 simulated lenses are considered passing. Passing lenses demonstrate a mean η of 0.94 and $\sigma_{eta} = 0.016$, a mean f_{actual} of 125.13 μm with $\sigma_{focal} = 71.50$ nm, and a mean FWHM of 99.11 nm with $\sigma_{fwhm} = 9.94$ nm. The maximum efficiency demonstrated is 0.96 with any greater efficiency values corresponding to FWHMs larger than the allowable focal spot size. Partitioning the MC into categories allows analysis of the trends between the various errors. Figure 5 illustrates the correlation matrix for paired error types in the passing lens category. It should be noted that increasing the minimum η required for passing lenses exaggerates the correlation values between errors, i.e., as the minimum allowable η for a passing lens increases, the correlation between post-polish height and imprint depth increases.

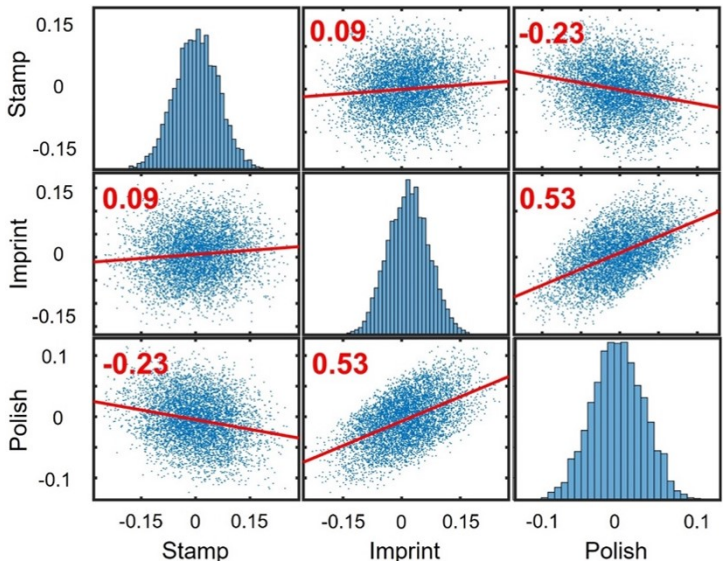

Fig. 5. The correlation matrix for the MC ($3\sigma = 0.18$) passing lenses with $\eta \geq 0.9$ with a FWHM ≤ 1 μm. The histograms in the diagonal depict the population of the various errors while the off diagonals demonstrate the Pearson correlation coefficients for the paired errors after outliers have been removed.

3.3. Neural network aided Monte Carlo analysis

The traditional MC analysis performed in Section 3.2 is computationally demanding owing to the need to perform many FDTD simulations. This makes it challenging to repeat the analysis for arbitrary sets of process conditions and error distributions. To address this issue and to enable predictive performance analysis for an arbitrary set of stamp, imprint, and polishing error distributions, we employed neural network (NN) aided MC analysis. Here, we use the original MC data set with N = 5,000 ($3\sigma = 0.18$) as NN training data (50% training, 50% held back for validation) as illustrated in Fig. 6(a). The NN shown in Fig. 6(b) is implemented in JMP Pro with two hidden layers with six neurons each, where each layer consists of two neurons with tanh, linear, and Gaussian activation functions respectively. The resulting NN then allows for accurate prediction of the metalens focusing efficiency, η, for arbitrary combinations of stamp

Optical Materials EXPRESS

height, imprint depth, and polishing thickness error values – without requiring any additional FDTD simulations to be performed.

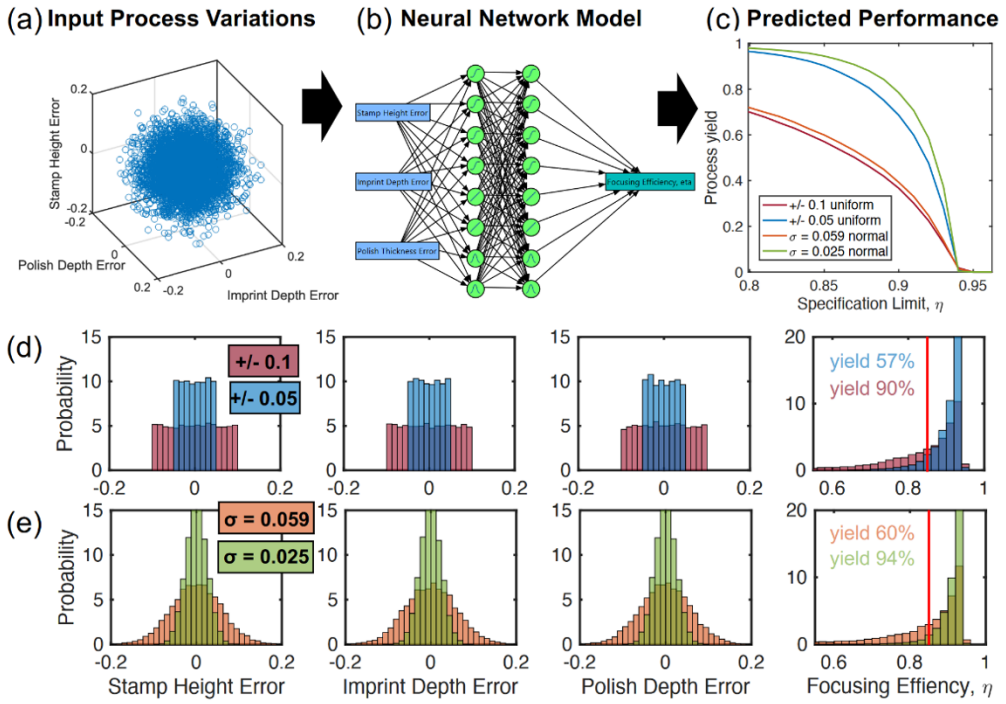

Fig. 6. (a) The MC results used to train the NN. (b) The NN architecture used to predict η using input error values. The activation functions used are depicted in the green circles representing the neurons with sigmoid functions shown in the top neurons, linear activation functions in the middle, and nonlinear activation functions shown at the bottom. (c) Yield predicted by the NN as minimum η for a passing lens is increased. (d) Uniform error distribution between error boundaries and the yield predicted using the error distribution for a minimum η of 0.9. (e) Normal error distribution using varying σ values for all three tested errors, as well as the yield predicted using the error distribution for a minimum η of 0.9.

As shown in Fig. 6(c), the NN can be utilized to perform on-demand MC analysis for any set of input error distributions (Fig. 6(d),(e)) effectively bypassing the need to perform thousands of FDTD simulations. This method enables direct and computationally efficient prediction of the process yield as a function of process capability as shown in Fig. 6. For example, if the specification limit for a 'passing lens' is set to $\eta = 0.85$, then the NN aided MC predicts process yields of 57% and 90% for uniformly distributed process capabilities, $|\Delta\kappa| < 0.1$ and $|\Delta\kappa| < 0.05$ respectively. The predicted yield improves to 60% and 94% for normally distributed process capabilities with $\sigma = 0.059$ and 0.025 respectively. In other words, if the process windows for stamp height, imprint depth, and polish thickness can all be controlled to +/- 7.5% variation (3σ) then ~94% of lenses should exhibit a focusing efficiency $\eta \geq 0.85$.

Lastly in Fig. 7 we visualize the NN model by plotting surface contours for various interdependent defects, while holding one constant. The results suggest that even higher process yields would be possible if the fabrication process is re-targeted or biased based on known errors. For example, adjustments in the targeted imprint depth or polish thickness can be used to compensate a stamp that is slightly too tall or shallow. Similarly, adjustments to the targeted polish thickness could also be used to compensate an imprint that was too deep or shallow. Intuitively, these

Optical Materials EXPRESS

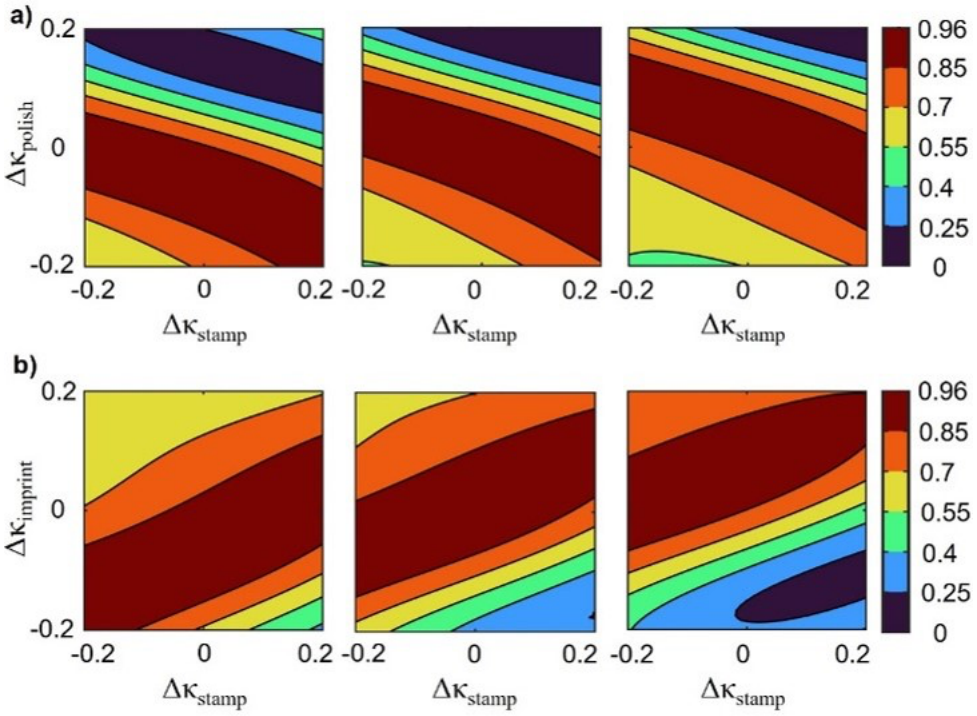

Fig. 7. (a) NN output describing the relationship between η, $\Delta\kappa_{stamp}$ and $\Delta\kappa_{polish}$ assuming $\Delta\kappa_{imprint} = -0.06$, $\Delta\kappa_{imprint} = 0$ and $\Delta\kappa_{imprint} = 0.06$, respectively. (b) NN output describing the relationship between η, $\Delta\kappa_{stamp}$ and $\Delta\kappa_{imprint}$ assuming $\Delta\kappa_{polish} = 0$, $\Delta\kappa_{polish} = -0.06$, and $\Delta\kappa_{polish} = 0.06$, respectively. The colorbars indicate the predicted η output.

results are consistent with the transmissive phase of the EMM metasurface, $\Delta\phi(n) = 2\pi/\lambda_0 \acute{D} n \times t$, which indicates the index contrast can be traded off with the post-planarization film thickness. We anticipate that similar results may be obtained in conventional meta-optics, wherein lateral variations in critical dimensions can be traded off with the thickness of the meta-atom device layer.

4. Conclusion

In this article, a novel fabrication method for producing planar EMMs operating at visible wavelengths – NIRI – is theoretically and numerically analyzed. The NIRI method represents a low-overhead, easily parallelized, high-resolution, high-throughput alternative to serial optics fabrication methods such as EBL and FIB. The NIRI technique requires only silicon wafers, an electrochemical wet bench, an appropriate master stamp and stamping press, and a polishing tool. We showed that the NIRI process is theoretically capable of producing high performance transmissive EMMs by imparting $\Delta\phi = 2\pi$ from pSi thin films nanoimprinted with an appropriately pre-mastered stamp. Moreover, we established a generalized method for designing such stamps requiring only an input arbitrary phase function and knowledge of the initial thickness and porosity of the pSi film to be imprinted. Lastly, we investigated in detail the effects of independent and interdependent fabrication variations stemming from errors in post-polish thickness, stamping depth, and/or stamp height; and showed how NN aided MC analysis is an effective tool for predicting process tolerances of EMMs. In the future, we anticipate that this framework can be

Optical Materials EXPRESS

utilized to design arbitrary flat-optics compatible with direct nanoimprinting of effective medium substrates.

Appendix: closed form solution for the required stamp profile

Equation (2) describes the stamp profile that is required to compress a porous substrate of starting thickness h_0 and porosity P_0 to a targeted porosity distribution $P(x,y)$. Here we assume a two component Bruggeman effective medium of the form:

$$P(x,y)\frac{\epsilon_1-\epsilon_2}{\epsilon_1+2\epsilon_2}+(1-P(x,y))\frac{\epsilon_2-\epsilon_{\text{eff}}(x,y)}{\epsilon_2+2\epsilon_{\text{eff}}(x,y)}=0, \tag{A1}$$

where ε_1, ε_2, and ε_{eff} are the relative permittivities of the void, skeleton, and initially uncompressed porous film respectively. Given Eq. (A1) and $n=\sqrt{\epsilon}$, the porosity distribution $P(x,y)$ can be expressed according to:

$$P(x,y)=\frac{-n_1^2n_2^2+n_1^2n_{\text{eff}}(x,y)^2-2n_2^2n_{\text{eff}}(x,y)^2+2n_{\text{eff}}(x,y)^4}{3n_{\text{eff}}(x,y)^2(n_1^2-n_2^2)} \tag{A2}$$

Then Eq. (2) can be re-expressed solely in terms of refractive indices, including the targeted refractive index profile $n_{eff}(x,y)$ and initial uncompressed film index $n_{\text{eff},0}$ according to:

$$s(x,y)=h_0\frac{n_1^2\cdot n_2^2\cdot n_{\text{eff},0}^2-n_1^2\cdot n_2^2\cdot n_{\text{eff}}(x,y)^2+2\cdot n_{\text{eff},0}^4\cdot n_{\text{eff}}(x,y)^2-2\cdot n_{\text{eff},0}^2\cdot n_{\text{eff}}(x,y)^4}{n_{\text{eff},0}^2\cdot(n_1^2\cdot n_2^2+2\cdot n_1^2\cdot n_{\text{eff}}(x,y)^2-n_2^2\cdot n_{\text{eff}}(x,y)^2-2\cdot n_{\text{eff}}(x,y)^4)}. \tag{A3}$$

Finally, the stamp design can be directly related to the phase profile, under the assumption of a perfectly linear phase vs. index response:

$$\Delta\phi(x,y)\approx\frac{2\pi}{\lambda_0}(n_{\text{eff}}(x,y)\ -\ n_{\text{eff},0})\ t, \tag{A4}$$

where the accuracy of this approximation is examined earlier in the discussion of Fig. 2(a). From Eq. (A4) the effective index profile required can be written as:

$$n_{\text{eff}}(x,y)\ \approx n_{\text{eff},0}+\frac{\lambda_0}{2\pi t}\ \Delta\phi(x,y). \tag{A5}$$

Thus a closed form solution for the stamp profile $s(x,y)$ is obtained from Eqs. (A3) and (A5).

Funding. Office of Naval Research (N00014-20-1-2558); National Science Foundation (1825787, 2047015).

Acknowledgments. M. P. acknowledges the generous support from the United States Department of Defense Science, Mathematics, and Research for Transformation scholarship program funded by OUSD/R&E, National Defense Education Program/BA-1 Basic Research.

Disclosures. The authors declare no conflict of interest.

Data availability. Data underlying the results presented in this paper are not publicly available at this time but may be obtained from the authors upon reasonable request.

References

1. M. Kadic, G. W. Milton, M. van Hecke, *et al.*, "3D metamaterials," Nat. Rev. Phys. **1**(3), 198–210 (2019).
2. J. Hu, S. Bandyopadhyay, Y. Liu, *et al.*, "A Review on Metasurface: From Principle to Smart Metadevices," Front. Phys. **8**, 1 (2021).
3. W. T. Chen, A. Y. Zhu, and F. Capasso, "Flat optics with dispersion-engineered metasurfaces," Nat. Rev. Mater. **5**(8), 604–620 (2020).
4. X. Xie, M. Pu, J. Jin, *et al.*, "Generalized Pancharatnam-Berry Phase in Rotationally Symmetric Meta-Atoms," Phys. Rev. Lett. **126**(18), 183902 (2021).

Optical Materials EXPRESS

5. R. Alaee, M. Albooyeh, and C. Rockstuhl, "Theory of metasurface based perfect absorbers," J. Phys. D: Appl. Phys. **50**(50), 503002 (2017).
6. Z. Ruan and S. Fan, "Superscattering of Light from Subwavelength Nanostructures," Phys Rev Lett **105**(1), 013901 (2010).
7. S. Tretyakov, "Maximizing Absorption and Scattering by Dipole Particles," Plasmonics **9**(4), 935–944 (2014).
8. W. Stork, N. Streibl, H. Haidner, *et al.*, "Artificial distributed-index media fabricated by zero-order gratings," Opt. Lett. **16**(24), 1921–1923 (1991).
9. A. A. Maznev and V. E. Gusev, "Waveguiding by a locally resonant metasurface," Phys. Rev. B **92**(11), 115422 (2015).
10. J. Van Kranendonk and J. E. Sipe, "V Foundations of the Macroscopic Electromagnetic Theory of Dielectric Media," in *Progress in Optics*, E. Wolf, ed. (Elsevier, 1977), 15, pp. 245–350.
11. S. Jahani and Z. Jacob, "All-dielectric metamaterials," Nat. Nanotechnol. **11**(1), 23–36 (2016).
12. A. I. Kuznetsov, A. E. Miroshnichenko, M. L. Brongersma, *et al.*, "Optically resonant dielectric nanostructures," Science **354**(6314), aag2472 (2016).
13. S. Wang, P. C. Wu, V.-C. Su, *et al.*, "A broadband achromatic metalens in the visible," Nat. Nanotechnol. **13**(3), 227–232 (2018).
14. S. W. D. Lim, M. L. Meretska, and F. Capasso, "A High Aspect Ratio Inverse-Designed Holey Metalens," Nano Lett. **21**(20), 8642–8649 (2021).
15. Irati Jáuregui-López, Pablo Rodriguez-Ulibarri, Sergei A. Kuznetsov, *et al.*, "THz sensing with anomalous extraordinary optical transmission hole arrays," Sensors **18**(11), 3848 (2018).
16. A. M. Shaltout, A. V Kildishev, and V. M. Shalaev, "Evolution of photonic metasurfaces: from static to dynamic," J. Opt. Soc. Am. B **33**(3), 501–510 (2016).
17. T. Gu, H. J. Kim, C. Rivero-Baleine, *et al.*, "Reconfigurable metasurfaces towards commercial success," Nat. Photonics **17**(1), 48–58 (2023).
18. P. Cheben, R. Halir, J. H. Schmid, *et al.*, "Subwavelength integrated photonics," Nature **560**(7720), 565–572 (2018).
19. S. Okazaki, "High resolution optical lithography or high throughput electron beam lithography: The technical struggle from the micro to the nano-fabrication evolution," Microelectron. Eng. **133**, 23–35 (2015).
20. A. Leitis, M. L. Tseng, A. John-Herpin, *et al.*, "Wafer-Scale Functional Metasurfaces for Mid-Infrared Photonics and Biosensing," Adv. Mater. **33**(43), 2102232 (2021).
21. B. Turkot, S. Carson, and A. Lio, "Continuing Moore's law with EUV lithography," in *2017 IEEE International Electron Devices Meeting (IEDM)* (2017), pp. 14.4.1–14.4.3.
22. M. Totzeck, W. Ulrich, A. Göhnermeier, *et al.*, "Pushing deep ultraviolet lithography to its limits," Nat. Photonics **1**(11), 629–631 (2007).
23. V. C. Su, C. H. Chu, G. Sun, *et al.*, "Advances in optical metasurfaces: fabrication and applications [invited]," Opt. Express **26**(10), 13148–13182 (2018).
24. D. K. Oh, T. Lee, B. Ko, *et al.*, "Nanoimprint lithography for high-throughput fabrication of metasurfaces," Frontiers of Optoelectronics **14**(2), 229–251 (2021).
25. S. Choi, J. Zuo, N. Das, *et al.*, "Scalable Nanoimprint Manufacturing of Multi-layer Metasurfaces for Compact Polarimetric Imaging System," in *2023 Conference on Lasers and Electro-Optics, CLEO 2023* (2023).
26. V. J. Einck, M. Torfeh, A. McClung, *et al.*, "Scalable Nanoimprint Lithography Process for Manufacturing Visible Metasurfaces Composed of High Aspect Ratio TiO2 Meta-Atoms," ACS Photonics **8**(8), 2400–2409 (2021).
27. J. Kim, J. Seong, W. Kim, *et al.*, "Scalable manufacturing of high-index atomic layer–polymer hybrid metasurfaces for metaphotonics in the visible," Nat. Mater. **22**(4), 474–481 (2023).
28. G. Yoon, K. Kim, D. Huh, *et al.*, "Single-step manufacturing of hierarchical dielectric metalens in the visible," Nat. Commun. **11**(1), 2268 (2020).
29. Daniel Werdehausen, *Nanocomposites as Next-Generation Optical Materials: Fundamentals, Design and Advanced Applications*, 1st ed. (Springer Nature, 2021).
30. S. Y. Chou, C. Keimel, and J. Gu, "Ultrafast and direct imprint of nanostructures in silicon," Nature **417**(6891), 835–837 (2002).
31. A. Sharstniou, S. Niauzorau, A. L. Hardison, *et al.*, "Roughness Suppression in Electrochemical Nanoimprinting of Si for Applications in Silicon Photonics," Adv. Mater. **34**(43), 1 (2022).
32. A. Sharstniou, S. Niauzorau, P. M. Ferreira, *et al.*, "Electrochemical nanoimprinting of silicon," Proc. Natl. Acad. Sci. U. S. A. **116**(21), 10264–10269 (2019).
33. W. I. Park, T. W. Park, Y. J. Choi, *et al.*, "Extreme-Pressure Imprint Lithography for Heat and Ultraviolet-Free Direct Patterning of Rigid Nanoscale Features," ACS Nano **15**(6), 10464–10471 (2021).
34. A. L. Hardison, T. H. Talukdar, I. I. Kravchenko, *et al.*, "Digital and Gradient Refractive Index Planar Optics by Nanoimprinting Mesoporous Silicon," Adv. Opt. Mater. **10**(24), 2201597 (2022).
35. T. H. Talukdar, J. C. Perez, and J. D. Ryckman, "Nanoimprinting of Refractive Index: Patterning Subwavelength Effective Media for Flat Optics," ACS Appl. Nano Mater. **3**(8), 7377–7383 (2020).
36. R. C. Devlin, M. Khorasaninejad, W. T. Chen, *et al.*, "Broadband high-efficiency dielectric metasurfaces for the visible spectrum," Proc. Natl. Acad. Sci. **113**(38), 10473–10478 (2016).
37. K. Ohta and H. Ishida, "Matrix formalism for calculation of electric field intensity of light in stratified multilayered films," Appl. Opt. **29**(13), 1952–1959 (1990).

Optical Materials EXPRESS

38. J. D. Ryckman, M. Liscidini, J. E. Sipe, *et al.*, "Direct imprinting of porous substrates," in OSA Technical Digest (CD), paper CMEE3 (Optica Publishing Group, 2011).
39. K. Li, A. Martins, S. Bohora, *et al.*, "Hybrid Metalens for Miniaturised Ultraviolet Fluorescence Detection," Adv. Opt. Mater. **11**(22), 2300852 (2023).
40. J. A. Cox, T. R. Werner, J. C. Lee, *et al.*, "Diffraction efficiency of binary optical elements," Proc.SPIE **1211**, 116–124 (1990).
41. G. J. Swanson, Binary Optics Technology: Theoretical Limits on the Diffraction Efficiency of Multilevel Diffractive Optical Elements (Lincoln Laboratory, Massachusetts Institute of Technology, 1991).